

Heavy flavor jet properties.

by

Xiao Wang

A dissertation submitted in partial satisfaction of the

requirements for the degree of

Doctor of Philosophy

in

in the

Graduate Division

of the

University of Illinois, Chicago

Committee in charge:

Olga Evdokimov, Chair

Summer 2020

Heavy flavor jet properties.

Copyright 2020

by

Xiao Wang

Contents

Contents	i
List of Figures	ii
List of Tables	iii
1 Introduction	1
1.1 The Standard Model	1
1.1.1 The Quantum Chromodynamics	3
1.1.2 Hadron Collisions and Factorization	4
1.1.3 QCD Branching , Hadronization and Jets	5
1.2 QCD Phase Transition and Quark-Gluon-Plasma	7
1.2.1 Relativistic heavy-ion collisions	8
1.2.2 Jet Quenching and Hard Probes	11
2 The CMS Detector	16
2.1 The CMS Tracker	17
2.2 The CMS Calorimeter Detector	19
2.2.1 Electromagnetic Calorimeter	20
2.2.2 Hadronic Calorimeter	21
2.3 The CMS Trigger System	23
Bibliography	25

List of Figures

1.1	The pictorial representation of the elementary particles of the standard model. .	2
1.2	The summary of the coupling constant measurements, as a function of the transverse momentum Q , from [1].	4
1.3	The energy density and the 3 times the pressure divided by the fourth power of the temperature of QCD matters. A cross over transition happened around $T = 170$ MeV and slowly converge to the Stefan-Boltzmann's law after $T > 500$ MeV [6].	9
1.4	The nuclear modification factor for inclusive charged particle produced in PbPb and pPb collisions measured by the CMS collaboration. The $R_{AA}(p_T) < 1$ for high p_T particles in PbPb collisions [18].	11
1.5	The transverse momentum ratio $X_{j\gamma}$ of p_T^{jet} to p_T^γ for differential centrality bins and compared with that in pp collisions [19]. The $X_{j\gamma}$ is almost the same in pp and peripheral PbPb collisions, but the $X_{j\gamma}$ shifted significantly to the soft sector in PbPb central collisions.	12
1.6	The schematic illustration of an energetic parton scattering process when medium presents, taking from [20]. The source term refers to the interaction from the QGP.	13
1.7	The ratio of the radial jet momentum distribution $P(\Delta r)$ of jets between PbPb and pp collisions for the indicated intervals of p_T^{trk} shown for the 0-10% (most central) bin. The shaded bands show the total systematic uncertainties [21]. . .	14
1.8	The splitting function in PbPb collisions shown in differential centrality bins and overlay with the smeared splitting function in pp collisions. Taken from [22]. . .	15
2.1	The schematic diagram of the LHC complex. Figure from CERN-Poster-2013-377.	17
2.2	The perspective view of the CMS detector [28].	18
2.3	The schematic diagram of the particle trajectory traveling through the CMS detector.	19
2.4	The schematic diagram of the positions of CMS tracker layers and disks in a $z-r$ plane. The blue lines refer to the "stereo" modules and the red lines are pixel layers and disks. Figure from [30]	20
2.5	The schematic view of the CMS ECAL in $y-z$ plane [32].	21
2.6	The schematic view of the CMS HCAL in $y-z$ plane [32].	22
2.7	The schematic diagram of the CMS trigger system [35].	23

List of Tables

Acknowledgments

I

Chapter 1

Introduction

To understand on how the universe we live works is one of the most profound desire of human being. And this leads to all the creations all over from the mythology in history to the science in nowadays. Today, we believe that we understand this question, in particularly under the atomic scale, more clear than anytime in our history. All these knowledge about the physics laws in this universe can be summaries into a theory we called "Standard model". Although, this theory has archieved a great experimental success ever, there are questions and curiosities are still waiting to be answered. Besides several fundamental assumptions of the model are yet to be validated, knowing the behavior of a dihydrogen oxide atom well is far from enough to understand the wave in a ocean. Likewise, the phenomenon emerging from the collection of these fundamental particles can be non-trivial for us.

1.1 The Standard Model

All the interactions we knew in the universe can be classified into four types: the electromagnetism, weak interactoin, the strong interaction and gravity. The standard model provides a theory to describe three of them except the gravity. Based on the standard model, the bricks of the universe are individalbe fermionic particles which can be grouped into two classes: "quarks" and "leptons". Besides, several types of bosonic particles are playing the role of the interaction carrier to connect all elementary particles for building up the mechine of the current universe. All types of elementary particles in the standard model are illustrated in the Fig. [1.1](#).

The standard model suggested to group quarks and leptons into three generations, 2 particles for each quark or lepton generation in order to form the $SU(2)$ doublets. Each

Standard Model of Elementary Particles

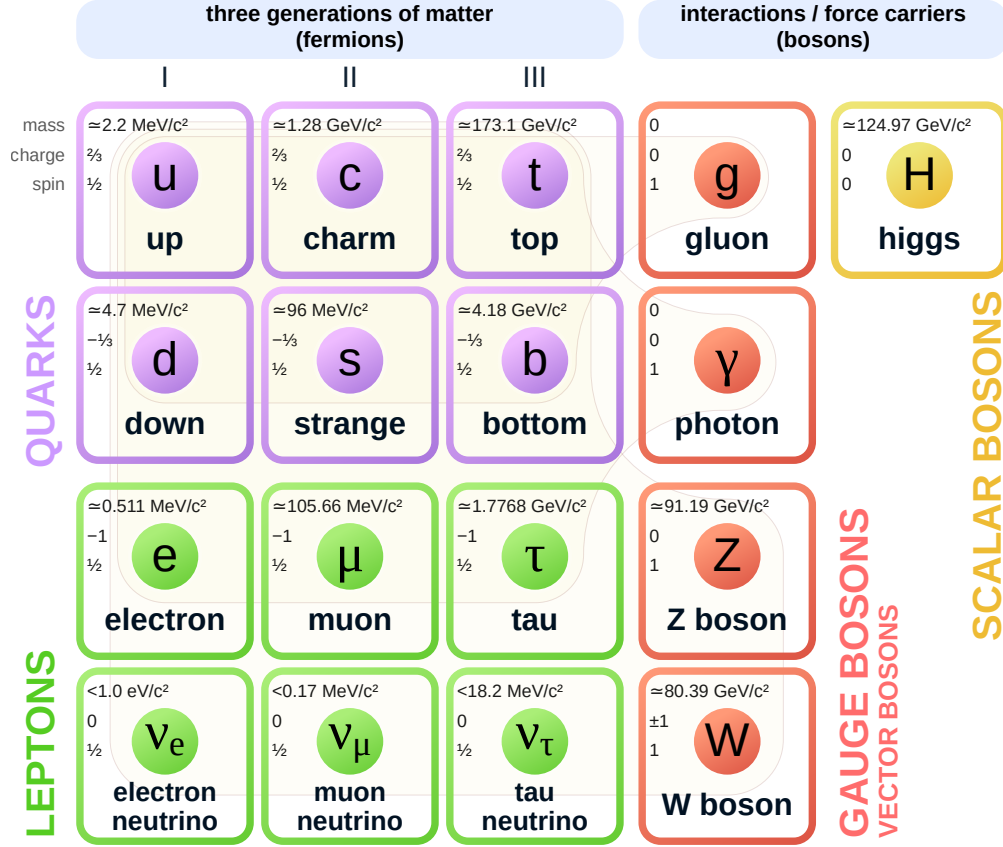


Figure 1.1: The pictorial representation of the elementary particles of the standard model.

of particles process the isospin, weak hyper charge, and hence the electric charge. Besides of these quantum number, quarks carries color charges while the leptons don't. It means that the lepton will not participate the strong interaction. Unlike the quarks, each lepton is combined with a corresponding electric neutral neutrino to form a $SU(2)$ doublet. The neutrinos are considered to be left-handed massless particles while the modern experimental suggests that the chirality might be broken for them. All the leptons and quarks have anti-particles which have opposite electric charge to the original except the neutrino is anti-particle of itself.

All the interactions are carried out by the gauge bosons: the photon γ for the electromagnetism, the vector bosons W^\pm and Z for the weak interaction, and finally the gluon g for the strong interaction. These gauge bosons corresponds to different gauge symmetries and only the electromagnetic $U(1)$ and colorful $SU(3)$ are preserved, so that the photon and

gluon are massless. This electromagnetism $U(1)$ symmetry is broken from a $SU(2) \times U(1)$ symmetry by the Higgs mechanism which leads to the massive Z and W^\pm . And this mechanism requires a non-vanished vacuum expectation of the Higgs field which is observed as the Higgs boson.

While the electroweak theory gave a unified description on the electromagnetism and the weak interaction, the strong interaction is described by the Quantum Chromodynamics (QCD) in the standard model. Although both of the two theories build upon the non-Abelian gauge field theory, the different symmetry assumption leads to very distinguish consequence.

1.1.1 The Quantum Chromodynamics

The Lagrangian of the QCD can be illustrated as the formula below:

$$\mathcal{L} = i\bar{\psi}^i \not{D}_i^j \psi_j - m\bar{\psi}^i \psi_i - \frac{1}{4} G_{\mu\nu}^a G_a^{\mu\nu}, \quad (1.1)$$

where the ψ^i are the quark fields and the $\not{D} = \gamma^\mu D_\mu$.

$$\begin{aligned} D_\mu &= \partial_\mu - i\frac{g_s}{2} G_\mu^a \lambda_a, \\ G_\mu^a &= \partial_\mu A_\nu^a - \partial_\nu A_\mu^a + gf^{abc} A_\mu^b A_\nu^c, \end{aligned} \quad (1.2)$$

where γ^μ are the Lorentz group, g_s is the coupling constant, A_μ^a are the gluon fields and f^{abc} are the structure constants of the $SU(3)$ group. Noticing the last term in the Lagrangian can leads to three or four self-coupling vertices for gluon fields. This feature not only increased the computation complexity for QCD processes, but also leads to unique QCD phenomenon.

The running coupling $\alpha_s(k^2)$ obtained from the one-loop renormalization is

$$\alpha_s(k^2) = \frac{4\pi}{\left(\frac{11N_C}{3} - \frac{2n_f}{3}\right) \ln\left(\frac{k^2}{\Lambda_{\text{QCD}}}\right)}, \quad (1.3)$$

leads to a feature that the coupling decreasing logarithmically as the k^2 raising, and this phenomenon is known as "asymptotic freedom". The $\Lambda_{\text{QCD}} \sim 200$ MeV which means that the coupling above this scale is expected to be weak (Fig. 1.2). This also implies that the coupling increasing with the decreasing of k and makes the perturbation expansion with respect to the order of the coupling constant failed. However, the numerical calculation from lattice QCD suggested that the coupling between quarks will increasing linearly as a function of r , the distance between two quarks. This may explain the fact that there's no free quark observed in nature so far. And this experience is summarized to a postulation that partons are confined inside hadrons.

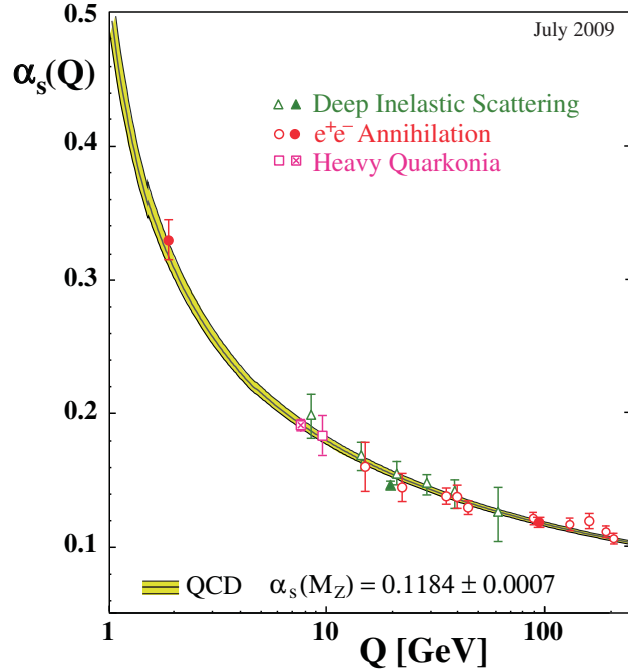


Figure 1.2: The summary of the coupling constant measurements, as a function of the transverse momentum Q , from [1].

1.1.2 Hadron Collisions and Factorization

The asymptotic free behavior leads to a simplification assumption that the collisions of two hadrons at high energy scale can be treated as the scattering of the partons from each of hadrons, like these partons are free relative to the rest constituents of the hadrons. This assumption works surprisingly well in deep inelastic scattering experiment. It suggests that the cross section of two hadrons h_1, h_2 to particles X can be expressed as

$$\begin{aligned} \sigma(h_1 h_2 \rightarrow X) = & \sum_{n=0}^{\infty} \alpha_s^n(\mu_R^2) \int dx_1 dx_2 f_{i/h_1}(x_1, \mu_F^2) f_{j/h_2}(x_2, \mu_F^2) \\ & \times \sigma_{ij \rightarrow X}^{(n)}(x_1, x_2, \mu_R^2, \mu_F^2) + \mathcal{O}, \end{aligned} \quad (1.4)$$

where $\alpha_s(\mu_R^2)$ is the coupling constant with the renormalization scale μ_R^2 , the $f_{i/h}(x, \mu_R^2)$ is the type i parton distribution function (PDF) inside the hadron h , x is the momentum fraction of the parton i inside the hadron, and the μ_F^2 is an arbitrary $\overline{\text{MS}}$ renormalization scale. However, this function can only be extracted from experiment or be calculated numerically based on DGLAP evolution. $\sigma_{ij \rightarrow X}^{(n)}$ is the n -th order of the cross section of the process $ij \rightarrow X$. The higher order represents the non-perturbation contributions.

The particles X could be partons, however, due to the strong coupling of partons in long ranges, it is believed that the partons will be created and recombined together to form color singlet particles like hadrons. In that sense, the partons will continuous splitting into the partons through the QCD allowed vertices.

Suppose $f_{i/h}(x, \mu_F^2)$ stands for the amplitude that finding a parton i from h carrying the z fraction of the energy of h , μ_F^2 is an arbitrary normalization scale impling that this distribution includes all the contributions less than the scale μ_F^2 . However, if the energy increased by ΔQ , then this distribution will needs to take the splitting contribution from the energy between μ_F^2 to $\mu_F^2 + \Delta Q$. This leads to the equation:

$$f_{i/h}(x, \mu_F^2 + \Delta Q) = f_{i/h}(x, \mu_F^2) + \frac{\alpha(\mu_F^2)}{2\pi} \sum_j P_{i \leftarrow j}(z) f_{j/h}(x/z, \mu_F^2), \quad (1.5)$$

where $P_{i \leftarrow j}(z)$ represents the amplitude of a parton i carried z fraction of energy with respect to the parent parton j . And this leads to the Altarelli-Parisi Equation:

$$\frac{\partial f_{i/h}(x, \mu_F^2)}{\partial \ln \mu_F^2} = \frac{\alpha(\mu_F^2)}{2\pi} \sum_j \int_x^1 \frac{dz}{z} P_{i \leftarrow j}(z) f_{j/h}\left(\frac{x}{z}, \mu_F^2\right), \quad (1.6)$$

where the splitting function can be obtained from pQCD order-by-order.

The energy of intial partons will be carried away by the branching partons until the energy fall below the branching threshold. The scattering between these partons will form into hadrons. The energy scale for this final stage is lower than the perturbative energy scale so that the higher order contriubtions are not negligible. The pQCD is no longer applicable in this stage so that we have to rely on some other models or effective theories.

1.1.3 QCD Branching , Hadronization and Jets

Thinking of the evolution of a single initial parton, it will branching into multiple partons with less energies individually and this branching process will mixing a hadronization in the end period. The final observation we will get are a bunch of hadrons spatially distributed inside a small cone due to conservation of the momentum required these hadrons move into a roughly same direction. This collective observation is conceptually refereed as a "jet". Based on this conception, the definition of a jet can be detailed. Although the algorithm for clustering of these hadrons produced from the initial parton can be different which leads to the jet definition isn't unique. The factorization theorem tell us that these hadrons are closely related to the initial partons as we shown in Eq. 1.4. In this case, the function

$f_{i/j}(z, \mu_F^2)$ can be understood as the fragmentation function and it still satisfies the DGLAP equation 1.6 with a splitting kernel $P_{i \leftarrow j}(z)$. The expression of this kernel depends on the theory applicable on the energy scale μ_F^2 [2].

The splitting kernels for the partons in tree level are:

$$\begin{aligned} P_{q \leftarrow q}(z) &= \frac{4}{3} \left[\frac{1+z^2}{(1-z)_+} + \frac{1}{3} \delta(1-z) \right], \\ P_{g \leftarrow q}(z) &= \frac{4}{3} \left[\frac{1+(1-z)^2}{z} \right], \\ P_{q \leftarrow g}(z) &= \frac{1}{2} [z^2 + (1-z)^2], \\ P_{g \leftarrow g}(z) &= 6 \left[\frac{1-z}{z} + \frac{z}{(1-z)_+} + z(1-z) + \left(\frac{11}{12} - \frac{n_f}{8} \right) \delta(1-z) \right], \end{aligned} \quad (1.7)$$

where the function $1/(1-z)_+$ is defined as:

$$\int_0^1 \frac{f(z)}{(1-z)_+} dz = \int_0^1 \frac{f(z) - f(1)}{(1-z)} dz. \quad (1.8)$$

Noticing that the singularity in the functions above are expected to be normalized when the higher order contributions are involved. The energetic parton will also lose energy by irradiating soft gluons. Suppose the $(d\sigma/d\Omega)_0$ stands for the cross section of the energetic parton production, with out considered the radiation. Then the summation over the soft gluon radiation will contribute a correction factor so that the measured cross section is

$$\begin{aligned} \left(\frac{d\sigma}{d\Omega} \right)_{\text{Phys.}} &= \left(\frac{d\sigma}{d\Omega} \right)_0 \times \exp \left\{ -\frac{\alpha}{\pi} f_{\text{IR}}(q^2) \log \left(\frac{-q^2}{\mu^2} \right) \right\} \\ &\approx \left(\frac{d\sigma}{d\Omega} \right)_0 \times \exp \left\{ -\frac{\alpha}{\pi} \log \left(\frac{-q^2}{m^2} \right) \log \left(\frac{-q^2}{\mu^2} \right) \right\} \end{aligned} \quad (1.9)$$

where the μ is a infrared cut-off and the approximation hold for $q^2 \gg m^2$. The coefficient f_{IR} is:

$$f_{\text{IR}}(q^2) = \int_0^1 \left(\frac{m^2 - q^2/2}{m^2 - q^2 x(1-x)} dx \right) - 1. \quad (1.10)$$

The double logarithmic correction factor is known as Sudakov form factor. The probability of soft-gluon emission probability from a quark Q is given by

$$d\sigma_{Q \rightarrow Qg} = \frac{\alpha_s}{\pi} C_F \frac{(2 \sin \theta/2)^2 d(2 \sin \theta/2)^2}{[(2 \sin \theta/2)^2 + \Theta^2]^2} \frac{d\omega}{\omega} (1 + \mathcal{O}(\Theta)), \quad (1.11)$$

where $\Theta = m_Q/E_Q \ll 1$ in relativistic case and C_F is a color factor for the quark Q . For the case $\theta \ll 1$, the cross section is approximated to

$$d\sigma_{Q \rightarrow Qg} \approx \frac{\theta^2 d\theta^2}{(\theta^2 + \Theta^2)^2} \frac{d\omega}{\omega}, \quad (1.12)$$

which is a double logarithmic approximation. This implies that the cross section is suppressed in the region that $\theta < \Theta = M_Q/E_Q$. This effect can be significant if the mass of the quark is heavy such as the bottom or top quark. This suppression is known as dead cone effect, and it leads to the depopulation and leading parton effect to heavy flavor jets [3].

1.2 QCD Phase Transition and Quark-Gluon-Plasma

We knew that a hadron is formed by the partons bundling by the strong interaction propagated through gluons. The effective potential between a pair of $q\bar{q}$ is approximated by

$$V(r) = -\frac{A \cdot \ln r}{r} + K \cdot r, \quad (1.13)$$

where r is the distance between the two quarks and A, K are constants [4]. The asymptotic freedom happens when $r \rightarrow 0$ and the color confinement ensured by the linear term in the potential. Based on this idea, the Bag model is proposed to describe the hadron energy phenomenologically: a hadron energy density should be almost constant within a certain region with radius R , the hadron size, while the energy decrease outside this region. Based on this idea, the energy density of a hadron is approximated by

$$E \propto R^3 \Lambda_B^4 + \frac{C}{r}, \quad (1.14)$$

where the second term comes from the potential. The mass of this hadron is given by minimum point of R in this equation: $M \sim 3\Lambda_B^4 R^3$. For a typical value $R \sim 1$ fm and $M \sim 1000$ MeV, the bag energy density is about $\Lambda^B \sim 200$ MeV.

The binding from strong coupling will be broken if the partonic kinematic energy inside of the hadron is large enough. Partons will be created along with the gluon string breaking and hence the degree of the partonic freedom will increase. This parton creation process will reduce the kinematic energy to form new bound states. But the baryon number is conservative in QCD interaction so that the QCD matter system can be described by a grand canonical ensemble $E - TS - \mu_B B$ where S, T, B, μ_B are the entropy, temperature, net baryon number, and the baryon chemical potential, respectively. The ensemble of these

hadrons formed a gas-like phase of hadrons and the Stefan-Boltzmann's law is applicable. However, if the energy density is keeping increasing, it will leads to the partonic density increases so that the mean free pass length is getting shorter. The screening effect from the saturated partons will weaken the confinement of the partons so that they might eventually be free. The lattice QCD calculation shows that the Stefan-Boltzmann's law is broken around the $T = 150$ MeV, Fig. 1.3. The raising entropy, which means extra number of the micro-states occurs, is contributed by the new degree of freedom from the de-confined partons. This non-trivial changes implies the system reaches a new phase known as quark-gluon plasma (QGP), analogous to the plasma discovered for electron and ions. The 4th power of temperature law is restored after $T > 500$ MeV due to the partons are completely free and no extra degree of freedom can be added into the system. After the phase transition, the effective potential $V_{QGP}(r)$ for $q\bar{q}$ is

$$V_{QGP}(r) = -\frac{C}{r} \exp\left(-\frac{r}{\lambda_D}\right), \quad (1.15)$$

where the $\lambda_D(T) \propto 1/T$ is the Debye screening length due to the color charges are surrounded by soft color particles, like the naked color charge disappeared. The string term disappears due to the confinement string is broken. The Debye screening length for $T > T_c$, where T_c stands for the critical temperature for QCD phase transition to happen, is about $\lambda_D \sim O(0.1)$ fm [5].

1.2.1 Relativistic heavy-ion collisions

The accelerator technique can be used to compress hundreds of atoms into a very small space to reach the critical temperature of QCD phase transition. The fixed target experiments performed at the Alternating Gradient Synchrotron (AGS) in Brookhaven and the Super Proton Synchrotron (SPS) at CERN are the first two experiments attempting to artificially create the QGP between 1986 and around 2000. The center-of-mass energy per nucleon pair $\sqrt{s_{NN}}$ is 10 GeV and 20 GeV at the AGS and SPS, respectively. These measurements shows the evidence of the fraction of strangeness hadron enhancement in the final production compared to smaller collision systems. Furthermore, the measurement from SPS observed the suppression of J/ψ meson yields [7] which is confirmed by the later measurements at Relativistic Heavy Ion Collider (RHIC). Furthermore, they also observed the yield suppression generally exists for all particles with high transverse momentum. These phenomenon is collectively summarized as "jet quenching" [8, 9, 10]. These evidence confirmed

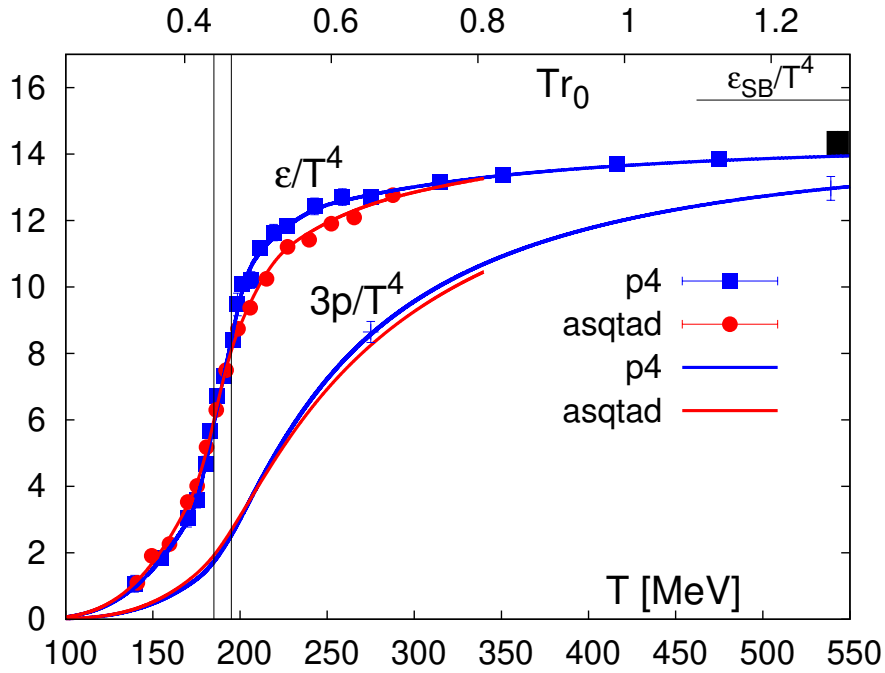


Figure 1.3: The energy density and the 3 times the pressure divided by the fourth power of the temperature of QCD matters. A cross over transition happened around $T = 170$ MeV and slowly converge to the Stefan-Boltzmann's law after $T > 500$ MeV [6].

that QGP can be and was created in the heavy-ion collisions. Another evidence comes from the measurement revealed a non-uniform soft particle momentum distribution as a function of the azimuthal angle ϕ which is known as elliptic flow [11]. This is a phenomenon often exists in a long range correlation dominated system described by hydrodynamics.

It is found that the Glauber model describes the hard processes in relativistic heavy-ion collisions well. Based on this model, a heavy-ion nuclei can be approximated by a bunch of nucleons superposition with respect to a nucleon wave function $\phi(r)$. The collision of two nuclei are considered as the collision of those two bunches of nucleons and the nucleon-nucleon interaction within the nuclei itself is ignored. Due to the Lorentz contraction, the collision of two ions is like the collision of the two discs with the centers offset by a distance from each other. We use a vector \mathbf{b} (impact parameter) originated from the center of ion A pointing to the center of ion B to quantify this collision geometry. The nucleon density of a ion A is rewritten into a thickness function $T_A(\mathbf{s})$ where the \mathbf{s} is the distance vector from the center to any point on the disc. Only those nucleons in the overlap region will participant

the collision and the number of them is noted as N_{part} . The probability $P(n, \mathbf{b})$ to have n hard collisions between ions A, B is given by the binomial distribution

$$P(n, \mathbf{b}) = \binom{AB}{n} \left[\hat{T}_{AB}(\mathbf{b}) \sigma_{\text{NN}}^{\text{intel}} \right]^n \left[1 - \hat{T}_{AB}(\mathbf{b}) \sigma_{\text{NN}}^{\text{intel}} \right]^{AB-n}, \quad (1.16)$$

where the $\sigma_{\text{NN}}^{\text{intel}}$ is the nucleon-nucleon cross section. The A, B are the nucleon number of each ions and the $T_{AB}(\mathbf{b})$ is the overlap thickness function defined as

$$\hat{T}_{AB}(\mathbf{b}) = \int d^2s \hat{T}_A(\mathbf{s}) \hat{T}_B(\mathbf{s} - \mathbf{b}). \quad (1.17)$$

The total nuclei-nuclei cross section σ_{NN} comes from summation over the binomial distribution

$$\sigma_{\text{NN}} = \int 2\pi b db \left\{ 1 - \left[1 - \hat{T}_{AB}(b) \sigma_{\text{NN}}^{\text{intel}} \right]^{AB} \right\}. \quad (1.18)$$

Further more, the number of the hard nucleon-nucleon collisions is given by

$$N_{\text{coll}}(b) = \sum_{n=0}^{AB} n P(n, \mathbf{b}) = AB \hat{T}_{AB}(b) \sigma_{\text{NN}}^{\text{intel}}, \quad (1.19)$$

where AB can be put into the overlapping function that $T_A B = AB \hat{T}_A B$.

The nucleon-nucleon cross section $\sigma_{\text{NN}}^{\text{intel}}$ is modeled the same way as 1.4 with a nucleon PDF(nPDF). The difference between the PDF and nPDF can result variety phenomenons like the color nuclear matter effects, for instance.

The different between the $\sigma_{\text{NN}}^{\text{intel}}$ and the free hadron cross section σ can be quantified by the ratio of the differential particle yield R_{AB} :

$$R_{AB}(x) = \frac{1}{\langle N_{\text{coll}} \rangle} \frac{dN^{AB}/dx}{dN^{pp}/dx} = \frac{1}{\langle T_{AB} \rangle} \frac{dN^{AB}/dx}{d\sigma/dx}, \quad (1.20)$$

where A, B stands for the type of the two colliding particles and x can be any observables like p_T, η, Ω , etc. It is worth to notice that the measurement of T_{AB} usually has less uncertainty than N_{coll} . A variety measurement on the nuclear modification factor of photon or W, Z bosons shows no significant difference between the $\sigma_{\text{NN}}^{\text{intel}}$ and σ for the electro-weak processes [12, 13, 14]. Because of the weak particles won't be affected significantly by the QGP which major involves strong interactions, these measurements proves that the Glauber model successfully described the collision geometry and the size of the hard scattering. Besides the effect from QGP, the nPDF of a nucleon is different from the same type of hadron. This difference can be extracted from the nuclear modification factor of other collision system such as R_{pA} or R_{eA} where the QGP effect is relatively small or negligible [15]. The relative modification of the hadron in nuclei can result the color nuclear matter effects [16].

1.2.2 Jet Quenching and Hard Probes

The typical size of the QGP is a few fm (estimated 6-11 fm at LHC) and the formation time of QGP is less than 1 fm/c [17] which implies that part of jets will path through this hot medium. As we mentioned previously, the $R_{AA}(p_T) = 1$ for weak particles like photon or Z bosons. However, as an example shown in the Fig 1.4, the $R_{AA}(p_T) < 1$ for high p_T particles and jets means the energy observed from these particles is relatively softer than those in pp collisions. Additionally, the imbalance study on photon-tagged jets in Fig. 1.5 shows that the jets lost energy in heavy-ion collisions.

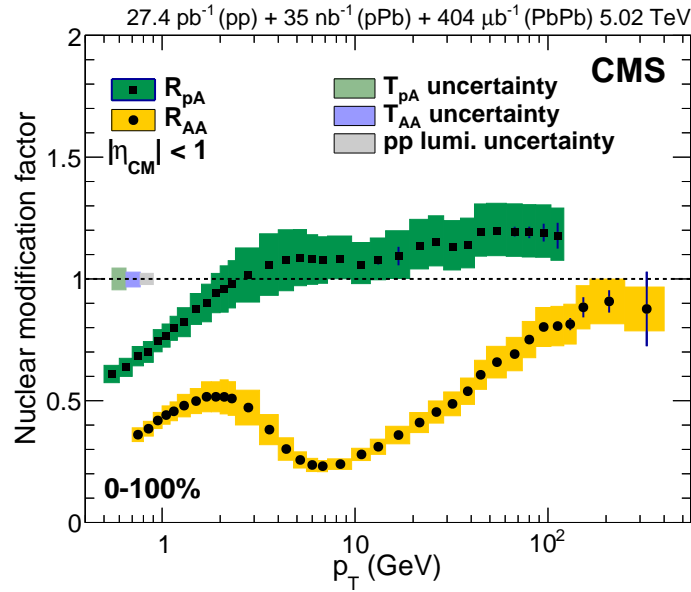


Figure 1.4: The nuclear modification factor for inclusive charged particle produced in PbPb and pPb collisions measured by the CMS collaboration. The $R_{AA}(p_T) < 1$ for high p_T particles in PbPb collisions [18].

Providing the fact that the jet production and evolution is well described by pQCD, these evidence not only prove that the QGP is created in heavy-ion collisions, but also allow us to use jets as probes to study the properties of this hot medium. Theoretically, the leading order term of the hard scattering in heavy-ion collisions can be obtained from the factorization

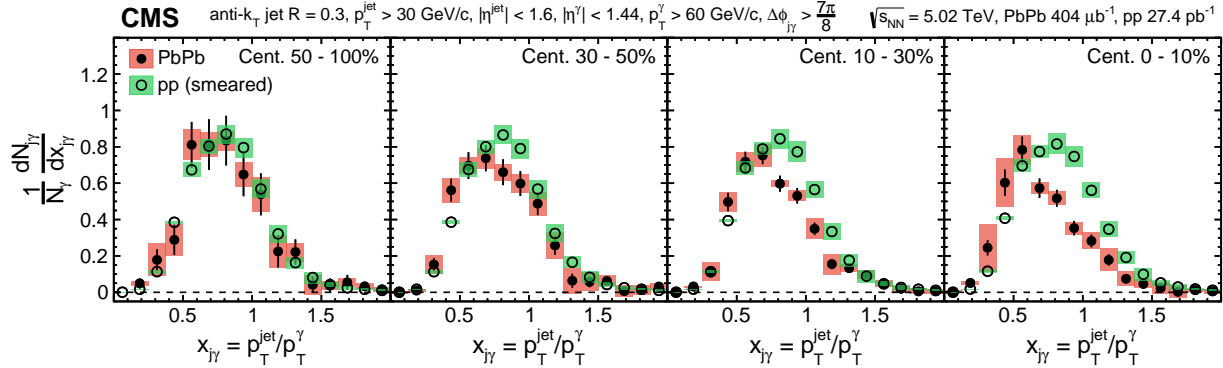


Figure 1.5: The transverse momentum ratio $X_{j\gamma}$ of p_T^{jet} to p_T^γ for differential centrality bins and compared with that in pp collisions [19]. The $X_{j\gamma}$ is almost the same in pp and peripheral PbPb collisions, but the $X_{j\gamma}$ shifted significantly to the soft sector in PbPb central collisions.

Eq. 1.4 with a modification term $\mathcal{P}(ab \rightarrow cd|T, u^\mu)$:

$$\begin{aligned}
 \sigma(h_1 h_2 \rightarrow X) &= \alpha_s(\mu_R^2) \int dx_1 dx_2 f_{i/h_1}(x_1, \mu_F^2) f_{j/h_2}(x_2, \mu_F^2) \\
 &\times \sigma_{ij \rightarrow ab}^{(1)}(x_1, x_2, \mu_R^2, \mu_F^2) \\
 &\times \mathcal{P}(ab \rightarrow cd|T, u^\mu) D_{X \leftarrow cd}(z_c, z_d, \mu_F^2),
 \end{aligned} \tag{1.21}$$

where the $D_{X \leftarrow cd}$ is the fragmentation function describing the hadrons X fragmented from energetic partons c, d , and T, u^μ stands for the temperature and the flow viscosity of the medium. The new term $\mathcal{P}(ab \rightarrow cd|T, u^\mu)$ stands for the probability amplitude of the partons a, b transfer into c, d due to the interaction with the medium (through a multi-scattering process illustrated in Fig. 1.6). Rather than that, the fragmentation term $D_{X \leftarrow cd}(z_c, z_d, \mu_F^2)$ maybe different from the case in vacuum. This fragmentation function still satisfies the DGLAP equation with a kernel of the parton interaction in medium which build a bridge to understand the QGP properties by studying the jet modification in heavy-ion collisions. z

Jet structure measurements can be used to constraint the branching kernel so that providing more detailed information to understand the QGP properties. The jet shape which is the jet constituent p_T distribution around the jet as a function of the distance of the constituent from the jet axis $r = \sqrt{(\Delta\eta)^2 + (\Delta\phi)^2}$, where $\Delta\eta = \eta_{\text{particle}} - \eta_{\text{jet}}$ and $\Delta\phi = \phi_{\text{particle}} - \phi_{\text{jet}}$ is measured for inclusive jets [21]. The comparison between the jet shapes in PbPb and pp shows that the energy has been shifted from higher p_T bin to lower bins, and the energy distributed in larger Δr region is higher than that in pp collisions. These modification shows clear centrality dependence which may related to the path length of the initiate parton of

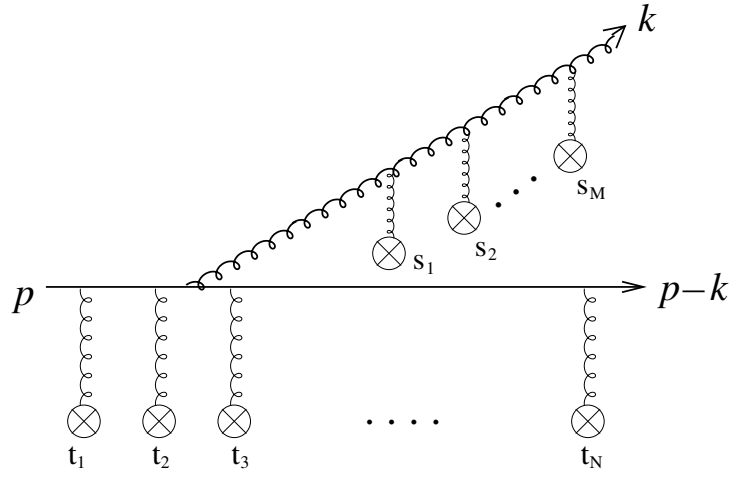


Figure 1.6: The schematic illustration of a energetic parton scattering process when medium presents, taking from [20]. The source term refers the interaction from the QGP.

the jet (Fig. 1.7).

The branching of the initial quarks will leads to one energetic jet split into two or more sub-jets carry portion of the energy from the original one. This process is a consequence phenomenon of the DGALP equation. This process should be infrared (IR) safe for the summation of all order of contribution but it is ill-defined to any certain order of α_s . With a jet grooming method, the IR unsafe part of the splitting function can be removed so that the rest part can be approximated by pQCD calculation. The observable splitting function is a distribution of function z_g

$$z_g = \frac{\min(p_{T1}, p_{T2})}{p_{T1} + p_{T2}}. \quad (1.22)$$

The measurement of z_g removed the soft splitting by the grooming condition $z_g > 0.1$ shows that the z_g distribution of the peripheral PbPb collisions is similar to the pp collisions which is well simulated by the PYTHIA and Herwig++ generator. However, the z_g in central PbPb collisions is modified to a softer splitting side (smaller z_g) comparing to pp collisions (Fig. 1.8).

The heavy flavor jets which are those jets initiated by a heavy flavor parton like, c, b or t quarks plays a unique role in the jet tomography probing the QGP properties. Because of the large mass of heavy flavor quarks, they are severely suppressed from the medium thermal production and will have to be created mainly from the very early hard scattering. The evolution of the heavy flavor jets will carry a full information of space-time profile and

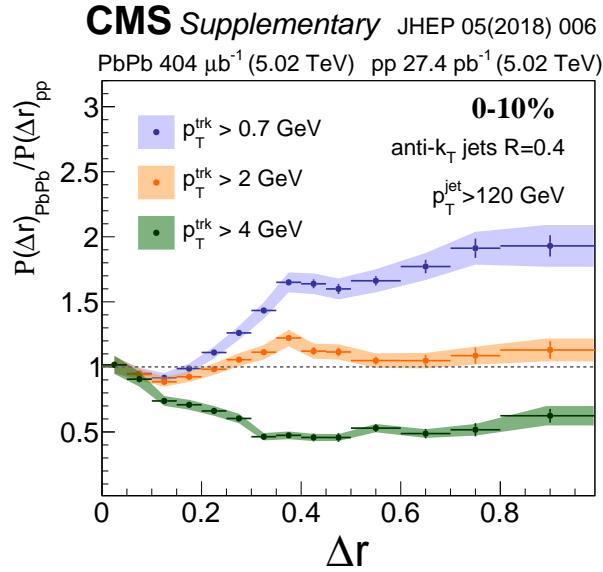


Figure 1.7: The ratio of the radial jet momentum distribution $P(\Delta r)$ of jets between PbPb and pp collisions for the indicated intervals of p_T^{trk} shown for the 0-10% (most central) bin. The shaded bands show the total systematic uncertainties [21].

the transportation properties of the QCD medium. Besides of this, the energy loss of the heavy flavor partons are expected to be less compared to the lighter partons due to the mass hierarchy. However, recent measurement shows a contradictory result: the jet imbalance study on b jet pairs show similar X_J distribution as inclusive jet pairs [23]. The suppression level of the prompt D meson nuclear modification factor R_{AA} is almost comparable with the inclusive charged particles [24]. These collective counter intuitive observation is collectively known as "heavy flavor puzzle". On the other hand, some heavy flavor jets can produced pairwise from a gluon splitting process. Although the splitting kernel is not IR safe but with grooming method, it can be a excellent observable to test the pQCD. Since some studies suggests the jet substructure might be very non-trivial in heavy ion collisions [25], It also can be used to test any potential changes of the pQCD in a finite temperature environment. More subtle heavy flavor jet structure measurements are needed to solve these questions.

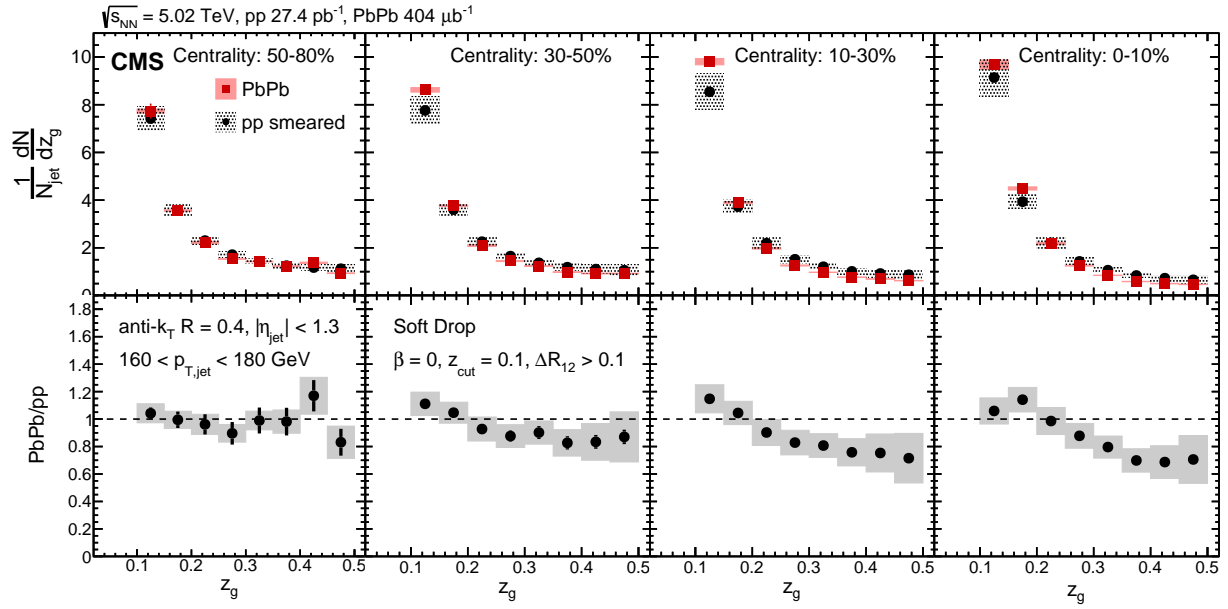


Figure 1.8: The splitting function in PbPb collisions shown in differential centrality bins and overlay with the smeared splitting function in pp collisions. Taken from [22].

Chapter 2

The CMS Detector

Particle accelerator is invited for artificially producing the hard collisions between particles to study not only the interaction between particles, but also probe the structure of the hadrons. The Large Hadron Collider (LHC) is the most power one that is still operating since 10 September 2008. It uses a multi-stage acceleration loops to boost proton or anti-proton beam reach to 6.5 TeV and collide two protons or anti-protons at the center-of-mass energy 13 TeV. Besides of the proton beam, it can also accelerates other type of ion beam and perform variety collisions such as proton-lead or lead-lead in lower center-of-mass energy per nucleon pair [26].

There are four detectors mounted at each of the 4 beam crossing points: Compact Muon Solenoid (CMS), A Toroidal LHC ApparatuS (ATLAS), Large Hadron Collider beauty (LHCb) and A Large Ion Collider Experiment (ALICE). The CMS and ATLAS are general purpose detector while the ALICE and LHCb are designed to specific experiments.

The LHC delivered proton beams reached the peak instance luminosity about $2.1 \times 10^{34} \text{ cm}^2\text{s}^{-1}$ in Run2. And reached three and a half more than designed luminosity in 2015 lead-lead collisions with a peak instance luminosity of $2.7 \times 10^{27} \text{ cm}^2\text{s}^{-1}$. LHC delivered 1.88 nb^{-1} inn 2018 lead-lead collisions at $\sqrt{s_{\text{NN}}} = 5.02 \text{ TeV}$ and CMS detector received 1.78 nb^{-1} with a peak instance luminosity of 6.4 Hz/mb. With the high instance luminosity, several hard collisions may happen in one bunch cross and this phenomenon is called "pileup" [27]. The number of the hard collisions per bunch crossing can reach about 60 in high luminosity proton run. However, the pileup is keeping very low in PbPb collisions due the particle multiplicity can be very high in PbPb hard collisions.

The CMS detector is a versatile particle detector consists by several sub-detectors: a pixel and strip based tracking system, a calorimeter system combined by a electromag-

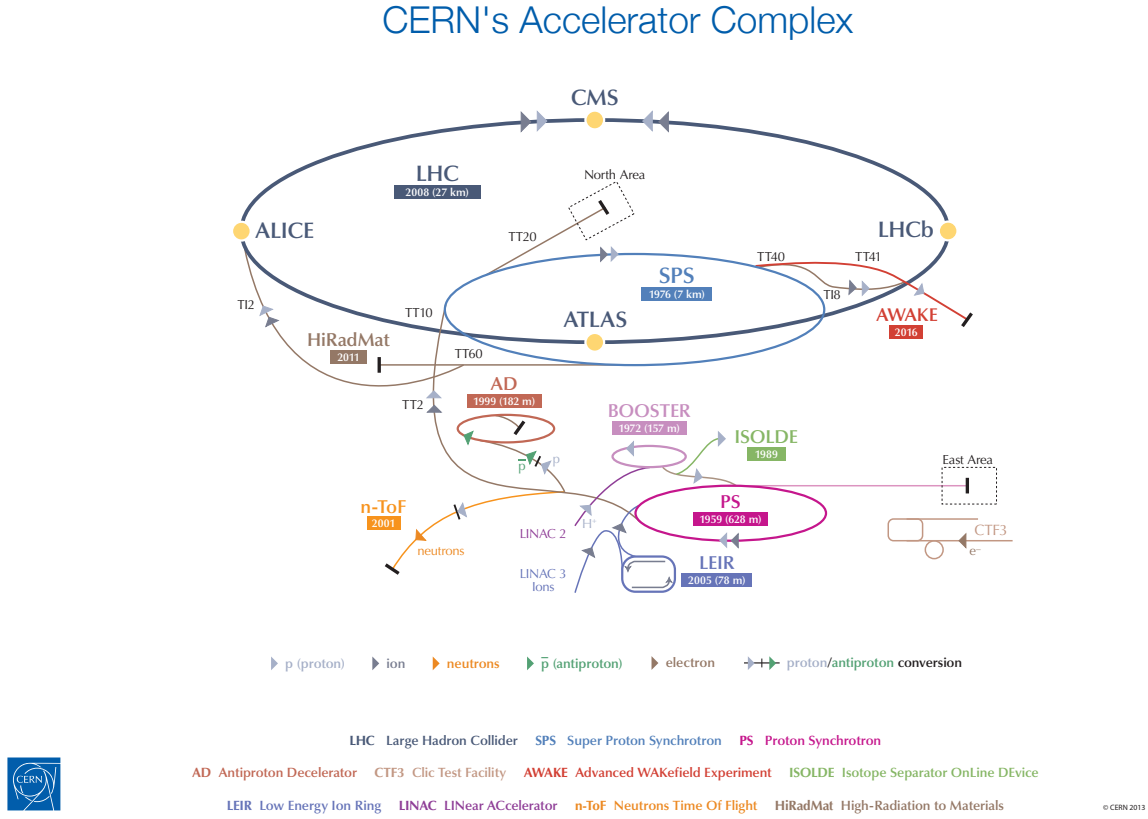


Figure 2.1: The schematic diagram of the LHC complex. Figure from CERN-Poster-2013-377.

netic calorimeter (ECal) followed by a hadronic calorimeter (HCal), and a superconducting solenoid magnet followed by muon detectors. The perspective of the CMS detector is illustrated in the Fig. 2.2. The schematic diagram of the trajectory of different types of particles traveling through the CMS detector is illustrated in the Fig. 2.3.

2.1 The CMS Tracker

The CMS tracker consists by a inner silicon pixel detector covered by a silicon strip detector. The original configuration of the tracker is illustrated in the Fig. 2.4. A right-handed coordinate is used in the CMS tracker. The origin point is at the collision point, x -axis points to the center of the LHC ring, a the y -axis pointing to the sky, and z -axis

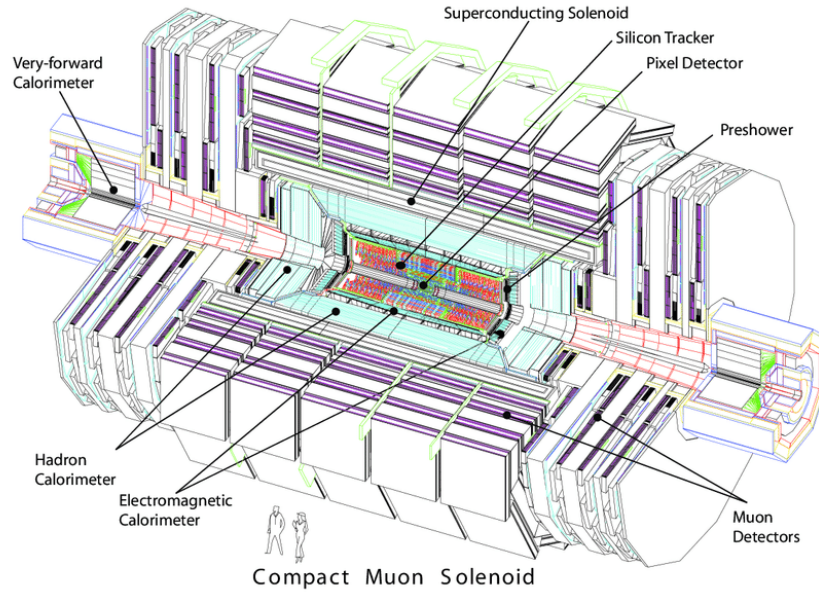


Figure 2.2: The perspective view of the CMS detector [28].

pointing to the anti-clockwise beam direction. The azimuthal angle ϕ measured in the $x-y$ plane with $\phi = 0$ refers to the x -axis.

The three concentric cylindrical barrel pixel layers are arranged at 4.3, 7.3 and 10.2 cm in radius away from the beam while the two forward pixel disks are placed at each side where $z = \pm 35.5$ and $z = \pm 48.5$ cm away from the collision points. One more layer is added to barrel and each side of forward after the phase-1 upgrade finished in 2017 [29]. This pixel detector is designed to provide a high precision three dimensional information of points left by the charged particle traveling through the silicon pixel. The barrel pixel provides a 4-hit efficient coverage in the region $|\eta| < 2.2$ and the forward pixel provides a 3-hit efficient coverage in the region $|\eta| < 2.5$. A 3.8 T magnetic field imposes a significant Lorentz force bending the charged particle trajectory to provides a better resolution for particles with different charge-to-mass ratio.

The CMS silicon strip detector is installed outside of the pixel detector. This strip detector consists by three major components: a Tracker Inner Barrel and Disk (TIB/TID) composed by 4 barrel layers and 3 forward disks, a Tracker Outer Barrel (TOB) consists of 6 layers and a Tracker EndCap (TEC) with 9 disks. The TIB strips placed parallel to the z direction and the disks of TID placed perpendicular to the z -axis can provides up to 4 r - ϕ measurements on one trajectory. The TIB/TID is surrounded by the TOB extended

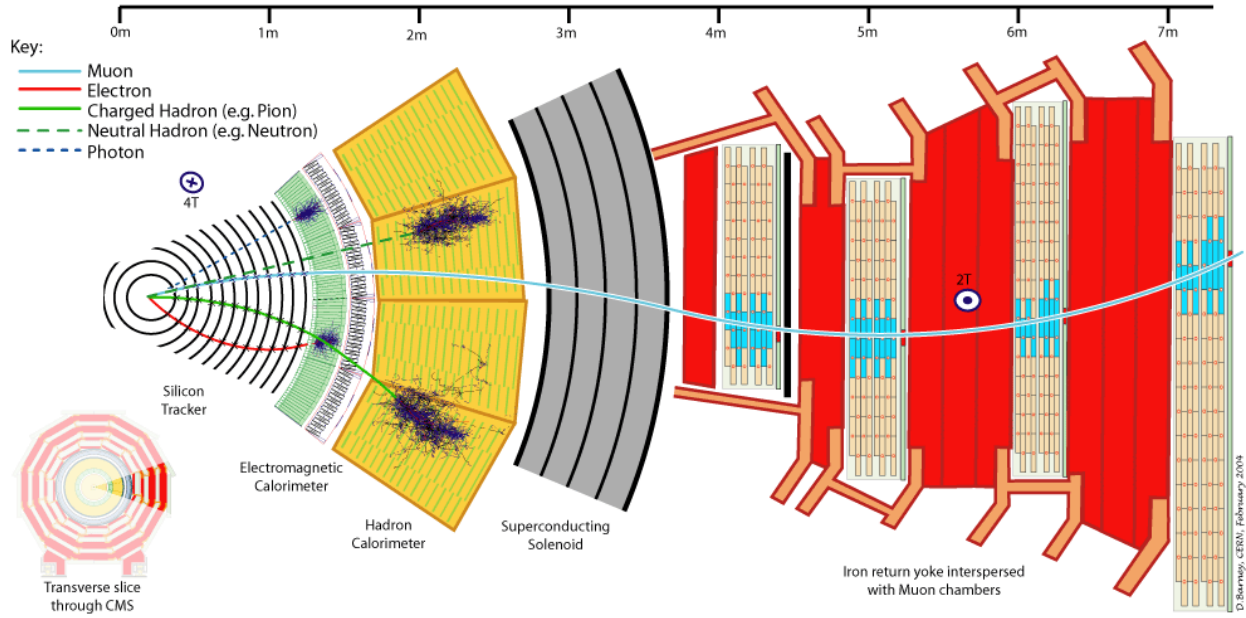


Figure 2.3: The schematic diagram of the particle trajectory traveling through the CMS detector.

to 116 in radius, and ± 118 cm in z direction. The disks of TEC are placed in the region $124 < |z| < 280$ cm on each side of TOB. Considering hits counted from stereo modules, the strip detector can provide from 8 to 14 efficient measurements of track impact points in the region $|\eta| < 2.4$ [31].

2.2 The CMS Calorimeter Detector

The calorimeter detector is designed to absorb all the incident particle energy so that it can provide efficient position and the energy information for those particles. The incident particles will interact with the material of calorimeter and shower cascades of secondary particles until all the energy has been absorbed by the material. The particles can be stopped by either electromagnetic interaction which cause the electromagnetic shower, or scattering from nucleons which cause the hadronic shower. The Electromagnetic Calorimeter (ECAL) and the Hadronic Calorimeter (HCAL) are designed to handle the two types of showers, separately.

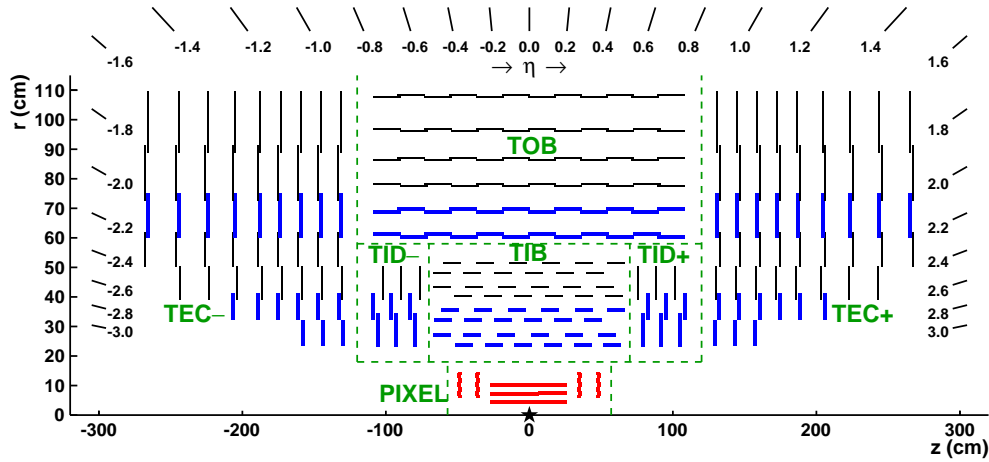


Figure 2.4: The schematic diagram of the positions of CMS tracker layers and disks in a $z - r$ plane. The blue lines refer to the "stereo" modules and the red lines are pixel layers and disks. Figure from [30]

2.2.1 Electromagnetic Calorimeter

ECAL placed outside of the CMS tracker is combined by a cylinder barrel consisted by a matrix of 61,200 PbWO_4 crystals and two flat "endcaps" sealed the two end side of barrel by about 15,000 extra crystals. The ECAL barrel (EB) with crystal size $22 \times 22 \text{ mm}^2$ in $\eta - \phi$ plane and 23 cm in depth provides a 1° azimuthal granularity covering the region $|\eta| < 1.48$ while the ECAL Endcaps (EE) cover the forward region $1.48 < |\eta| < 3.0$ by disks arranged $29 \times 29 \text{ mm}^2$ crystal [32]. Further more, a preshower (ES) detector made by lead and silicon sensors is placed in front of the ECAL EE to distinguish neutral pions in close spatial proximity, which usually decay into two photons. A schematic view of the CMS ECAL is shown in Fig. 2.5

The PbWO_4 that stopping the electrons and photon mainly through the bremsstrahlung and pair production, respectively, has a radiation length 0.89 cm which corresponds to a 2.2 cm Moliere radius. The 23 cm length (about 25.8 times of the radiation length) of PbWO_4 crystal can absorb approximately 98% of depth of particles showered from 1 TeV electrons. Associating the signal from adjusted crystals, the position of the high energy electrons can be determined in an accuracy of 0.5 mm, which allows matching the shower positions with the tracks reconstructed from the CMS tracker. However, the transparency of the crystal will decrease due to the thermal damage and irradiation dose it took. This makes the ECAL to be a destructive detector and the energy response of the ECAL is calibrated

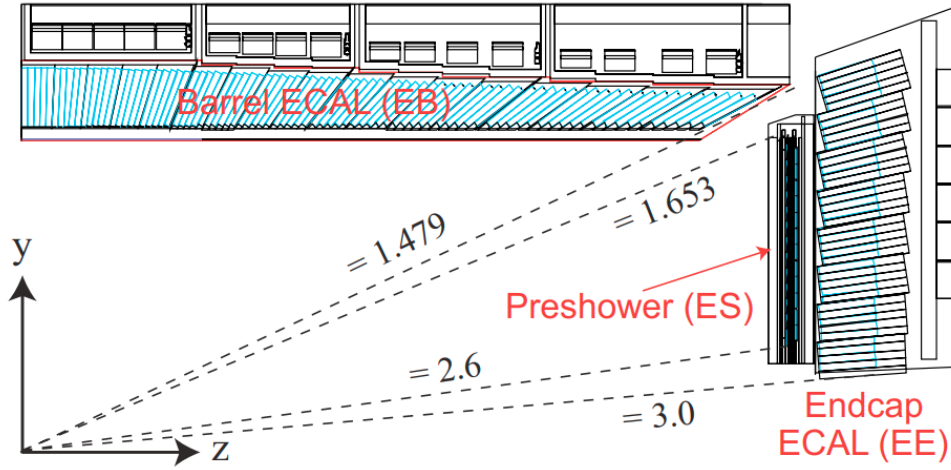


Figure 2.5: The schematic view of the CMS ECAL in $y - z$ plane [32].

periodically using the laser beam. The energy resolution of ECAL can be parameterized as

$$\left(\frac{\sigma}{E}\right)^2 = \left(\frac{S}{\sqrt{E}}\right)^2 + \left(\frac{N}{E}\right)^2 + C^2, \quad (2.1)$$

where the S, N, C stands for the stochastic, noise and constant term, respectively. For electrons with energy below 500 MeV, the resolution estimated by using a matrix of 3×3 crystals is parameterized as

$$\left(\frac{\sigma}{E}\right)^2 = \left(\frac{2.8\%}{\sqrt{E}}\right)^2 + \left(\frac{0.12}{E}\right)^2 + (0.30\%)^2, \quad (2.2)$$

where E is in GeV [28].

2.2.2 Hadronic Calorimeter

The CMS HCAL is a sampling calorimeter designed to measure the hadron energy by stopping and absorbing hadronic cascade showers produced from the incident hadrons. It lies between the ECAL and the CMS solenoid, and consists by four sub-detectors: the Hadronic Barrel (HB), Hadronic Endcap (HE), Hadronic Outer (HO) and Hadronic Forward (HF) calorimeters. The HB composed by 18 wedges, each cover 20° in ϕ , placed outside of the ECAL barrel to cover the $|\eta| < 1.4$ region. Each of the HB wedges covered by stainless steel uses 18 layers of brass as absorber interleaved with 17 plastic scintillator. The HO is made by brass disks, interleaved with scintillators which cover 20° in ϕ to cover forward

region $1.3 < |\eta| < 3.0$. The thickness of HB at $\eta = 0$ is about 5.8 hadronic interaction length and increase to 10 interaction length at $|\eta| = 1.2$. Each segment of the HCAL is aligned to a 5×5 crystal matrix in ECAL. The HB and HE calorimeters have granularity $\Delta\eta \times \Delta\phi = 0.087 \times 0.087$ for the region $|\eta| < 1.6$ and $\Delta\eta \times \Delta\phi = 0.175 \times 0.175$ for the region $1.6 < |\eta| < 3.0$. Energy leakage from HB and HE is supposed by captured by the HO consisted by 12-fold scintillator layers.

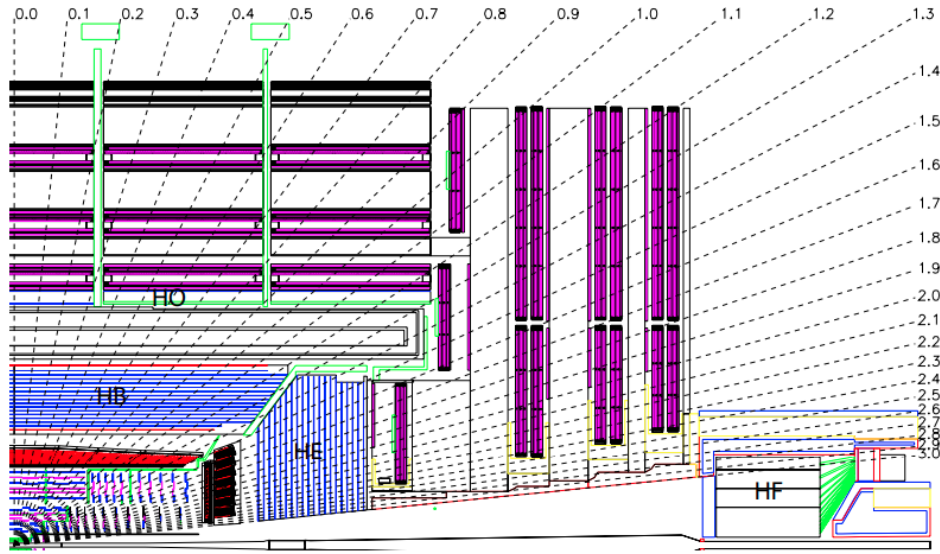


Figure 2.6: The schematic view of the CMS HCAL in $y - z$ plane [32].

The HF extends the calorimeter to a very space like proximity region $3.0 < |\eta| < 5.0$ where enormous radiation fluences shade on, typically in a Grad dose level. It consists by steel absorber and the quartz fiber Cherenkov Calorimeters which utilize the Cherenkov radiation produced by the shower charged particles in fiber to measure the energy of those electromagnetic showers. The advantage of this design is not only the quartz fiber tolerates to this high dose of radiation, but also the Cherenkov radiation is produced essentially simultaneously to makes a fast response in HF. The HF is a cylindrical steel structure with length 165 cm, outer radius 130 cm and inner radius 12.5 cm. There are 18 absorber wedges, each one covers 20 degree in azimuthal angle, placed in each side of the CMS interaction point. The two sizes of quartz fibers are alternate in nearby grooves space by 5 mm inserted into the absorber parallel to the z direction: a short length fiber only go through the first 22 cm from the front of the absorber while the long length fiber go all the way through the

absorbers. This arrangement allows the HF to distinguish the electromagnetic shower energy from the hadronic showers since electrons and photon typically starts shower at a relatively long depth in the absorber and hence leaves signal mainly on long fibers while the signal of hadronic showers can be detected in both length of fibers [33]. The HF segmentation is 0.175×0.175 for $|\eta| < 4.7$ and 0.175×0.35 for $|\eta| > 4.7$ [34]. The schematic organization of the HB, HE, HO and HF is shown in Fig. 2.6.

2.3 The CMS Trigger System

The collision rate delivered by LHC can reach 1 GHz. With an estimation of about 1 MeV per event record, it is not practice to store all the events for analyzing. Therefore, a two-stage sophisticated trigger system is used to promptly identify the interest event to recording. The first staged is a hardware based Level 1 Trigger (L1) and multiple software-based High-Level Triggers (HLT) form the second stage. The architecture of the CMS trigger system is illustrated in Fig. 2.7.

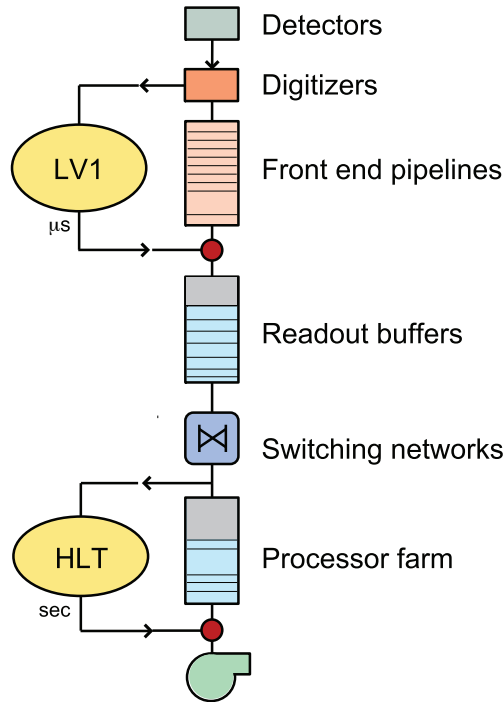


Figure 2.7: The schematic diagram of the CMS trigger system [35].

The L1 which made out of Filed-Programmable Gate Arrays (FPGAs) and Application Specific Integrated Circuits (ASICs) to limit the latency within $1\ \mu\text{s}$ for response is designed to reduce the event rate to 100 kHz at the LHC designed instance luminosity $\mathcal{L} = 10^{34}\ \text{cm}^2\text{s}^{-1}$. The total latency of the L1 is fixed at $3.2\ \mu\text{s}$ as the signal transition consumes a lot of time. Therefore the L1 system uses coarser granularity and lower resolution information (comparing to the signal from the front-end-electronics) from the calorimeters and muon chambers to search the energy deposit or hits for deciding whether this event should be kept. The full event information from front-end-electronics stand-by in pipelines will be collected and send to readout buffer once the the L1 selected the event. A switching network will distribute the data from readout to the HLT computing nodes (known as "Event Filter Farm") which are PCs mounting 2.66 GHz dual quad-core Intel processors accomplish with 16 GB RAM. The HLT algorithm is the modified offline reconstruction algorithm, which has improved processing speed, to produce high level physics object, like tracks and jets, for precisely identifying the event of interests and further reducing the event rate to the order of 100 Hz.

The event data selected from different HLTs will be streamed to corresponding dataset. However, due to the recording bandwidth limitation, not all events past the L1+HLT can be kept. A prescale scheme is adapted to feasibly adjust the fraction of events selected from different HLTs: a HLT with a prescaled rate n implies that one event will be recorded for every n events past this HTL. The events with the prescale number 1 is called unprescaled events. The final survived event will be store and reconstructed in offline computing center. The raw data and the reconstruction output will be transfered to the data center for long term storage.

Bibliography

- [1] Siegfried Bethke. “World Summary of $\alpha(s)$ (2011)”. In: *Nucl. Phys. B Proc. Suppl.* 222-224 (2012). Ed. by Guenter Grindhammer et al., pp. 94–100. DOI: [10.1016/j.nuclphysbps.2012.03.010](https://doi.org/10.1016/j.nuclphysbps.2012.03.010).
- [2] B. R. Webber. “Fragmentation and hadronization”. In: *eConf C990809* (2000). Ed. by J. Jaros and Michael E. Peskin, pp. 577–606. DOI: [10.1142/S0217751X00005334](https://doi.org/10.1142/S0217751X00005334). arXiv: [hep-ph/9912292](https://arxiv.org/abs/hep-ph/9912292).
- [3] Yuri L. Dokshitzer, Valery A. Khoze, and S. I. Troian. “On specific QCD properties of heavy quark fragmentation (‘dead cone’)”. In: *J. Phys. G* 17 (1991), pp. 1602–1604. DOI: [10.1088/0954-3899/17/10/023](https://doi.org/10.1088/0954-3899/17/10/023).
- [4] Simon Hands. “The Phase diagram of QCD”. In: *Contemp. Phys.* 42 (2001), pp. 209–225. DOI: [10.1080/00107510110063843](https://doi.org/10.1080/00107510110063843). arXiv: [physics/0105022](https://arxiv.org/abs/hep-ph/0105022).
- [5] K. Kajantie et al. “Nonperturbative Debye mass in finite temperature QCD”. In: *Phys. Rev. Lett.* 79 (1997), pp. 3130–3133. DOI: [10.1103/PhysRevLett.79.3130](https://doi.org/10.1103/PhysRevLett.79.3130). arXiv: [hep-ph/9708207](https://arxiv.org/abs/hep-ph/9708207).
- [6] A. Bazavov et al. “Equation of state and QCD transition at finite temperature”. In: *Phys. Rev. D* 80 (2009), p. 014504. DOI: [10.1103/PhysRevD.80.014504](https://doi.org/10.1103/PhysRevD.80.014504). arXiv: [0903.4379 \[hep-lat\]](https://arxiv.org/abs/hep-lat/0903.4379).
- [7] Ulrich W. Heinz and Maurice Jacob. “Evidence for a new state of matter: An Assessment of the results from the CERN lead beam program”. In: (Jan. 2000). arXiv: [nucl-th/0002042](https://arxiv.org/abs/nucl-th/0002042).
- [8] J. Adams et al. “Direct Observation of Dijets in Central Au+Au Collisions at $\sqrt{s_{NN}}=200\text{ GeV}$ ”. In: *Physical Review Letters* 97.16 (2006). ISSN: 1079-7114. DOI: [10.1103/physrevlett.97.162301](https://doi.org/10.1103/physrevlett.97.162301). URL: <http://dx.doi.org/10.1103/PhysRevLett.97.162301>.

- [9] J. D. Bjorken. “Energy Loss of Energetic Partons in Quark - Gluon Plasma: Possible Extinction of High $p(t)$ Jets in Hadron - Hadron Collisions”. In: (Aug. 1982).
- [10] A. Adare et al. “Transverse momentum and centrality dependence of dihadron correlations in Au+Au collisions at $\sqrt{s_{NN}} = 200$ -GeV: Jet-quenching and the response of partonic matter”. In: *Phys. Rev. C* 77 (2008), p. 011901. DOI: [10.1103/PhysRevC.77.011901](https://doi.org/10.1103/PhysRevC.77.011901). arXiv: [0705.3238 \[nucl-ex\]](https://arxiv.org/abs/0705.3238).
- [11] K. H. Ackermann et al. “Elliptic flow in Au + Au collisions at $(\sqrt{s_{NN}})^{1/2} = 130$ GeV”. In: *Phys. Rev. Lett.* 86 (2001), pp. 402–407. DOI: [10.1103/PhysRevLett.86.402](https://doi.org/10.1103/PhysRevLett.86.402). arXiv: [nuc1-ex/0009011](https://arxiv.org/abs/nuc1-ex/0009011).
- [12] Albert M Sirunyan et al. “The production of isolated photons in PbPb and pp collisions at $\sqrt{s_{NN}} = 5.02$ TeV”. In: *JHEP* 07 (2020), p. 116. DOI: [10.1007/JHEP07\(2020\)116](https://doi.org/10.1007/JHEP07(2020)116). arXiv: [2003.12797 \[hep-ex\]](https://arxiv.org/abs/2003.12797).
- [13] Georges Aad et al. “Z boson production in Pb+Pb collisions at $\sqrt{s_{NN}} = 5.02$ TeV measured by the ATLAS experiment”. In: *Phys. Lett. B* 802 (2020), p. 135262. DOI: [10.1016/j.physletb.2020.135262](https://doi.org/10.1016/j.physletb.2020.135262). arXiv: [1910.13396 \[nucl-ex\]](https://arxiv.org/abs/1910.13396).
- [14] Georges Aad et al. “Measurement of W^\pm boson production in Pb+Pb collisions at $\sqrt{s_{NN}} = 5.02$ TeV with the ATLAS detector”. In: *Eur. Phys. J. C* 79.11 (2019), p. 935. DOI: [10.1140/epjc/s10052-019-7439-3](https://doi.org/10.1140/epjc/s10052-019-7439-3). arXiv: [1907.10414 \[nucl-ex\]](https://arxiv.org/abs/1907.10414).
- [15] A. Kusina et al. “nCTEQ15 - Global analysis of nuclear parton distributions with uncertainties”. In: *PoS DIS2015* (2015), p. 041. DOI: [10.22323/1.247.0041](https://doi.org/10.22323/1.247.0041). arXiv: [1509.01801 \[hep-ph\]](https://arxiv.org/abs/1509.01801).
- [16] Michele Arneodo. “Nuclear effects in structure functions”. In: *Phys. Rept.* 240 (1994), pp. 301–393. DOI: [10.1016/0370-1573\(94\)90048-5](https://doi.org/10.1016/0370-1573(94)90048-5).
- [17] Fu-Ming Liu and Sheng-Xu Liu. “Quark-gluon plasma formation time and direct photons from heavy ion collisions”. In: *Phys. Rev. C* 89.3 (2014), p. 034906. DOI: [10.1103/PhysRevC.89.034906](https://doi.org/10.1103/PhysRevC.89.034906). arXiv: [1212.6587 \[nucl-th\]](https://arxiv.org/abs/1212.6587).
- [18] Vardan Khachatryan et al. “Charged-particle nuclear modification factors in PbPb and pPb collisions at $\sqrt{s_{NN}} = 5.02$ TeV”. In: *JHEP* 04 (2017), p. 039. DOI: [10.1007/JHEP04\(2017\)039](https://doi.org/10.1007/JHEP04(2017)039). arXiv: [1611.01664 \[nucl-ex\]](https://arxiv.org/abs/1611.01664).
- [19] Albert M Sirunyan et al. “Study of jet quenching with isolated-photon+jet correlations in PbPb and pp collisions at $\sqrt{s_{NN}} = 5.02$ TeV”. In: *Phys. Lett. B* 785 (2018), pp. 14–39. DOI: [10.1016/j.physletb.2018.07.061](https://doi.org/10.1016/j.physletb.2018.07.061). arXiv: [1711.09738 \[nucl-ex\]](https://arxiv.org/abs/1711.09738).

- [20] Sangyong Jeon. “Jet Quenching in Evolving QGP Medium”. In: *Nucl. Phys. A* 830 (2009). Ed. by Paul Stankus et al., pp. 107C–114C. DOI: [10.1016/j.nuclphysa.2009.10.012](#). arXiv: [0907.4691 \[nucl-th\]](#).
- [21] Albert M Sirunyan et al. “Jet properties in PbPb and pp collisions at $\sqrt{s_{\text{NN}}} = 5.02$ TeV”. In: *JHEP* 05 (2018), p. 006. DOI: [10.1007/JHEP05\(2018\)006](#). arXiv: [1803.00042 \[nucl-ex\]](#).
- [22] Albert M Sirunyan et al. “Measurement of the Splitting Function in pp and Pb-Pb Collisions at $\sqrt{s_{\text{NN}}} = 5.02$ TeV”. In: *Phys. Rev. Lett.* 120.14 (2018), p. 142302. DOI: [10.1103/PhysRevLett.120.142302](#). arXiv: [1708.09429 \[nucl-ex\]](#).
- [23] Albert M Sirunyan et al. “Comparing transverse momentum balance of b jet pairs in pp and PbPb collisions at $\sqrt{s_{\text{NN}}} = 5.02$ TeV”. In: *JHEP* 03 (2018), p. 181. DOI: [10.1007/JHEP03\(2018\)181](#). arXiv: [1802.00707 \[hep-ex\]](#).
- [24] Albert M Sirunyan et al. “Nuclear modification factor of D^0 mesons in PbPb collisions at $\sqrt{s_{\text{NN}}} = 5.02$ TeV”. In: *Phys. Lett. B* 782 (2018), pp. 474–496. DOI: [10.1016/j.physletb.2018.05.074](#). arXiv: [1708.04962 \[nucl-ex\]](#).
- [25] Hai Tao Li and Ivan Vitev. “Inverting the mass hierarchy of jet quenching effects with prompt b -jet substructure”. In: *Phys. Lett. B* 793 (2019), pp. 259–264. DOI: [10.1016/j.physletb.2019.04.052](#). arXiv: [1801.00008 \[hep-ph\]](#).
- [26] “LHC Machine”. In: *JINST* 3 (2008). Ed. by Lyndon Evans and Philip Bryant, S08001. DOI: [10.1088/1748-0221/3/08/S08001](#).
- [27] Albert M Sirunyan et al. “Pileup mitigation at CMS in 13 TeV data”. In: *JINST* 15.09 (2020), P09018. DOI: [10.1088/1748-0221/15/09/P09018](#). arXiv: [2003.00503 \[hep-ex\]](#).
- [28] S. Chatrchyan et al. “The CMS Experiment at the CERN LHC”. In: *JINST* 3 (2008), S08004. DOI: [10.1088/1748-0221/3/08/S08004](#).
- [29] W. Adam et al. “The CMS Phase-1 Pixel Detector Upgrade”. In: *JINST* 16.02 (2021), P02027. DOI: [10.1088/1748-0221/16/02/P02027](#). arXiv: [2012.14304 \[physics.ins-det\]](#).
- [30] Serguei Chatrchyan et al. “Description and performance of track and primary-vertex reconstruction with the CMS tracker”. In: *JINST* 9.10 (2014), P10009. DOI: [10.1088/1748-0221/9/10/P10009](#). arXiv: [1405.6569 \[physics.ins-det\]](#).
- [31] “Tracking and Vertexing Results from First Collisions”. In: (2010).

- [32] G. L. Bayatian et al. “CMS Physics: Technical Design Report Volume 1: Detector Performance and Software”. In: (2006).
- [33] A. Penzo and Y. Onel. “The CMS-HF quartz fiber calorimeters”. In: *J. Phys. Conf. Ser.* 160 (2009). Ed. by M. Fraternali, Gabriella Gaudio, and Michele Livan, p. 012014. DOI: [10.1088/1742-6596/160/1/012014](https://doi.org/10.1088/1742-6596/160/1/012014).
- [34] S Chatrchyan et al. “Performance of the CMS Hadron Calorimeter with Cosmic Ray Muons and LHC Beam Data”. In: *JINST* 5 (2010), T03012. DOI: [10.1088/1748-0221/5/03/T03012](https://doi.org/10.1088/1748-0221/5/03/T03012). arXiv: [0911.4991](https://arxiv.org/abs/0911.4991) [[physics.ins-det](#)].
- [35] S Chatrchyan et al. “Commissioning of the CMS High-Level Trigger with Cosmic Rays”. In: *JINST* 5 (2010), T03005. DOI: [10.1088/1748-0221/5/03/T03005](https://doi.org/10.1088/1748-0221/5/03/T03005). arXiv: [0911.4889](https://arxiv.org/abs/0911.4889) [[physics.ins-det](#)].